Molecular dynamics simulation and nonlinear analysis of density fluctuations in Lennard-Jones fluid system near the critical point

Yan Wang [a,b], Jinliang Xu [a,b,c,*], Qingyang Wang [a,c]

[a] *Beijing Key Laboratory of Multiphase Flow and Heat Transfer for Low Grade Energy Utilization, North China Electric Power University, Beijing, 102206, China*
[b] *Beijing Huairou Laboratory, Beijing, 101400, China*
[c] *Key Laboratory of Power Station Energy Transfer Conversion and System, North China Electric Power University, Ministry of Education, Beijing, 102206, China*

ARTICLE INFO

ABSTRACT

Spatiotemporal density is important to understand the fluid behavior especially near the critical point (NCP). Here, molecular dynamics (MD) was applied to investigate Lennard-Jones (LJ) fluid NCP. Periodic boundary conditions are applied on the six surfaces of a simulation box (SB) consisting of 10976 LJ fluid atoms. A slice of 3.45σ is selected in the SB, where σ is the length scale of the LJ fluid. Our results show that the time dependent densities in the slice obviously deviate from the average value in SB. The deviations are found to display M-shape distribution with increases of average densities. The maximum deviation occurs at $0.8\rho_c$ instead of at ρ_c, where ρ_c is the density at the critical point. Attention is paid on the phase distribution in the SB. Three regimes of liquid-like, two-phase-like and gas-like are observed to evolve with time. The density variation is explained by the combined effect of potential induced mechanism and critical fluctuation mechanism. The time series of densities in the slice behave either chaotic or random characteristics. The sample entropy in chaotic system is smaller than that in random system. Our work is helpful to understand the density variation and phase distribution in simple LJ fluid system when crossing the critical point.

1. Introduction

Supercritical fluid (SF) has been widely used in a variety of industrial fields including chemical engineering, materials sciences, and power engineering [1–4]. For applications such as multiphase chemical reactors [1,5], thermochemical conversion of biomass [6,7], wastewater treatment [8], material synthesis [2], and power generation [3,4], the advantageous properties of SF enable improved performance of these systems. For example, the intermolecular distance in SF is larger than that of traditional fluids at room temperature, allowing fast diffusion of solvent and low fluid viscosity which are beneficial for extraction and separation of useful product [9]. The large specific heat, high thermal conductivity, and low viscosity of SF are also favorable properties enabling their application in insulation of electronic equipment [10,11]. In textbooks, SF is regarded as a single-phase and homogeneous fluid and in the supercritical region, liquid and gas phases cannot be distinguished [12,13]. Recently, this concept is questioned by physicists. It was found that in SF, the distribution of molecules is not homogeneous, and fluctuations exist for the local density [14,15]. The properties

of SF is mainly resulted from the nonuniform distribution of molecules [16]. Therefore, in order to provide fundamental understanding of SF to improve and guide their applications in various industries, it is of great importance to study the microscale structure and dynamic behavior of SF.

Experimental studies of SF are expensive due to high pressure/temperature environment encountered. Measurement of SF parameters such as densities in short length and time scale becomes challenging [17,18]. However, molecular dynamics (MD) simulation is cost-effective to investigate the fluid behavior in short length and time scale [19]. MD simulations have been widely used to study the thermodynamic and transport phenomena of SF. It has shown that MD could produce reliable and reasonable results when intermolecular interactions and boundary conditions of the simulated system are properly treated [20–25]. In nature, molecules are divided into single-atom molecule such as argon and Xenon, as well as multi-atoms molecule such as water. For the former, simple LJ potential describes the interactions between molecules, which significantly reduces the computation time. The calculated results are sufficiently accurate to compare with experiments. For the latter, not only van der Waals force induced by the LJ potential between molecules, but also other forces such as coulomb force, should be considered. Hence, the computation time is much longer than the single atom fluid. In this paper, simple LJ fluid is applied.

The Mie potential energy is a simple expression to assess a number of properties [26]

$$\phi = \frac{C_k}{r^k} - \frac{C_l}{r^l} \tag{1}$$

where ϕ is the potential with $k>l$. The first term and second term represent repulsions and attractions, respectively. The most widely used intermolecular potentials is the Lennard-Jones (LJ) 12-6 potential [27]

$$\phi(r) = 4\varepsilon\left(\left[\frac{\sigma}{r}\right]^{12} - \left[\frac{\sigma}{r}\right]^{6}\right) \tag{2}$$

where ε is the depth of the attractive well, and σ is length scale for interactions between molecules, r is the distance between two neighboring molecules. The LJ type $r^{-\nu}$–$r^{-\mu}$ pair potentials were proposed in 1925 by Jones to describe the cohesive energy of crystals of noble gases, such as argon [28]. The current LJ 12-6 form was proposed by Lennard-Jones in 1931 after London had derived that the dispersion interaction between atoms decays as r^{-6} [29]. Latter, it was shown that the LJ 12-6 potential is not a particularly good pair potential. After Wood and Parker and, subsequently, performed the first Monte Carlo (MC) simulations, and Rahman performed the first Molecular Dynamics (MD) simulations, these simulations showed good agreement between simulation results and experimental data [30,31]. The reason is due to a fortuitous cancellation of errors [32]. Then, the LJ 12-6 potential has been widely used in various fields including physics, mechanics, and chemistry [33–35]. Wang et al. [35] presented a review on the intermolecular potential for various applications.

Density fluctuations are observed in nanoscale by Carlès [36]. Fluctuations are more serious near the critical point. Maddox et al. [37] simulated two-dimensional LJ fluid at densities below or near the critical point. They found that when approaching the critical point, the nonuniformity degree of densities increase, and the collective fluctuation and reconstruction time decrease. Based on the coordinate number of atoms, Martinez et al. [38] identified three regions of low, average and high densities in a two-dimensional LJ fluid system, and noted that the spatiotemporal densities of SFs fluctuate significantly. Yoshii et al. [39] performed MD simulations of LJ fluid xenon along the isothermal line of $1.07T_c$ with densities in the range of $(0.125-2.78)\rho_c$ where T_c and ρ_c are the critical temperature and critical density, respectively. At ρ_c, atomic clusters are observed to form large voids between clusters. Idrissi et al. [40] studied the heterogeneous structure of argon with temperatures below, near, and above the critical point. The results show that at temperatures below the critical point, the density is non-uniform because of the fluctuation of boundary atoms. At temperature close to the critical point, the density distribution becomes more non-uniform. At temperature higher than the critical point, the density inhomogeneity is weakened. Metatla et al. [41] studied the heterogeneous structure of supercritical water along different isothermal lines. Due to the combined effect of short-range force, indirect intermolecular force and hydrogen bonds, supercritical water can be seen as a mixture containing high-density fluid region and low-density region. The heterogeneity is more obvious as the average density decreases. When the average density is in the range of $(0.6-0.8)\rho_c$, the deviation of the local density from the average value reaches maximum [42].

It is noted that available studies on SF presented the atomic snapshot in static manner [39–41]. These studies describe the non-uniform distribution of SF, qualitatively. Different from the studies reported in the literature, this paper presents an investigation of spatial-temporal distribution of the LJ fluid near the critical point. The studied problem is important, due to many unusual phenomena taking place when a fluid is crossing the critical point. For example, heat transfer either can be enhanced, or can be deteriorated when a fluid is crossing the critical fluid, compared with heat transfer when the fluid is far away from the critical point. Another application involves the wastewater treatment in supercritical pressure, under which the chemical reaction rate is enhanced when the fluid is crossing the critical point [43,44].

In this paper, we performed MD simulations for LJ fluid near the critical point. Because the fluid near the critical point demonstrates two-phase-like characteristic, nonlinear analysis is introduced for the study. Average densities for the simulations are in the range of $(0.5-1.4)\rho_c$, along the critical isotherm $T=T_c$. The fluid density is averaged over a thin slice in the simulation box, but it is strongly time dependently. Probability density analysis and square root error are applied to analyze the time dependent density deviating from the average density. The deviations are found to display M-shape distribution with increasing average densities, and the maximum deviation appears at $\rho_{ave}=0.8\rho_c$. In the whole simulation box, the fluid is observed to have three-regimes of liquid-like (LL), two-phase-like (TPL) and gas-like (GL). The phase distribution of the three regimes is presented versus time. The nonlinear analysis

shows that with continuous increase of the average densities, the fluid displays the characteristics of random and chaotic, respectively. The random characteristic is shown with the average densities either at $0.5\rho_c$ or at $1.4\rho_c$. Chaotic fluid is observed when the fluid density is in the range of $(0.6\text{-}1.3)\rho_c$.

2. Simulation method

NIST is a widely used software to determine the physical properties for pure or mixture fluid. The software was developed by National Institute of Standards and Technology of USA. Each working fluid is based on a specific model cited from recognized reference. The argon model for the physical properties is based on Ref. [45], showing good accuracy when comparing with experiments. At the critical point for argon, the temperature, pressure and density are T_c=150.687 K, P_c=4.863 MPa and ρ_c=0.5356 g/cm^3 respectively, decided by the NIST software. Alternatively, the MD simulations by Michels et al. [46] gave T_c=150.86 K, P_c=4.834 MPa and ρ_c=0.5354 g/cm^3, respectively. It is seen that the NIST software determined values matched the MD simulation results well, with the maximum deviation between them less than 0.6%. In the present paper, the NIST software is used to determine the critical point of argon and arrange the running parameters of pressure, temperature and density for our studies.

They are written in non-dimensional form as $T_c^* = k_B T_c/\varepsilon = 1.2458$, $P_c^* = P_c \sigma^3/\varepsilon = 0.11496$ and $\rho_c^* = \rho_c \sigma^3/m = 0.31877$, respectively, where k_B is the Boltzmann constant, m is the mass of a molecule. Fig. 1a shows the *P-T* phase diagram in non-dimensional form. This figure is plotted based on the calculated data using the NIST software. The black curve represents the solid-liquid transition boundary (the melting line). The blue curve is the saturation line, on which a pressure corresponds to a saturation temperature in subcritical domain. The red curve is the Widom line in supercritical domain, determined by the maximum specific heat method. Fig. 1b helps to understand the determination process. At a supercritical pressure P^*, there is a temperature T^* at which the specific heat attains maximum. The Widom line is the collection of various data points of (T^*, P^*), see Fig. 1b. In this paper, all the MD simulations were performed at the critical temperature T_c. The pressures are varied in the range of $(0.920\text{-}1.056)P_c$, corresponding to the average
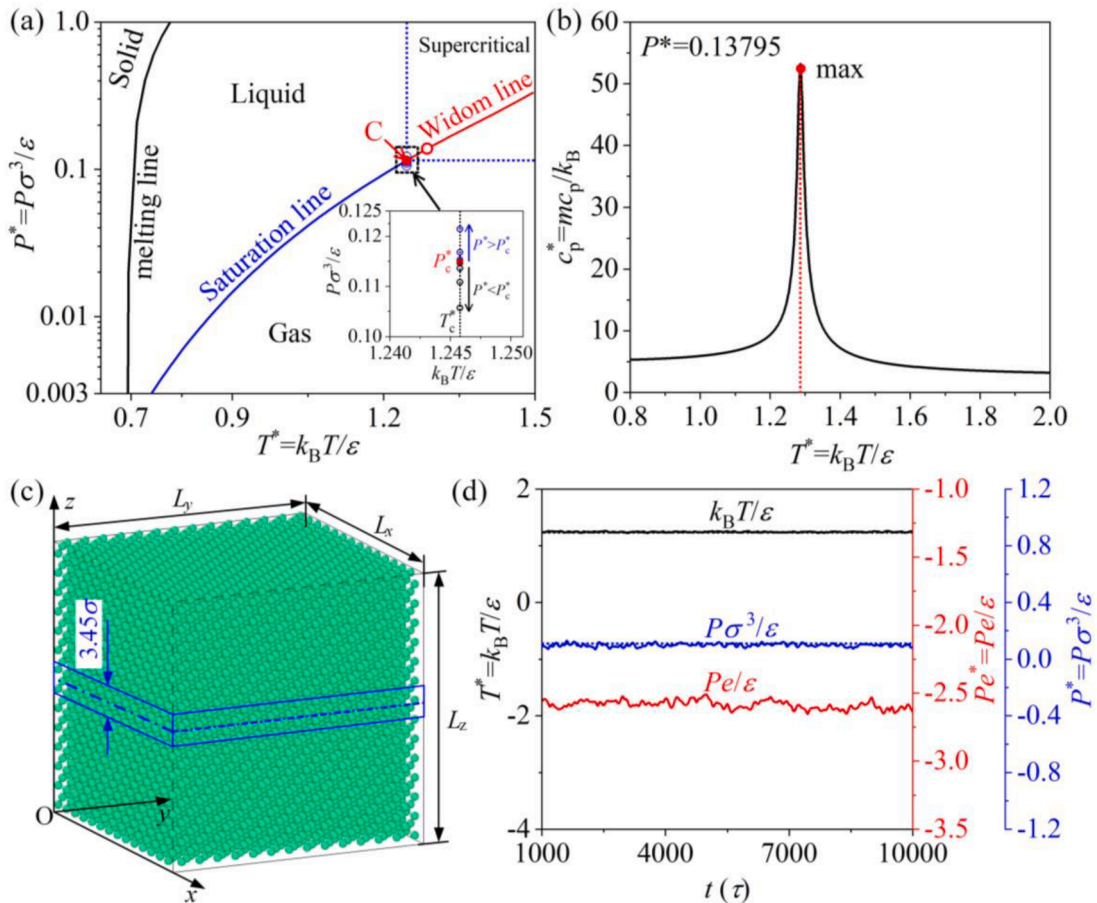
Fig. 1. MD simulation NCP. (a) the phase diagram for argon including subcritical domain and supercritical domain; (b) the determination of P^* and T^* based on the maximum specific heat method, with an example point shown at $P^* = 0.13795$; (c) the simulation box including a slice bin with a thickness of 3.45σ in SB; (d) the system temperatures and pressures versus time during early transition stage and steady stage for the fluid at the critical point.

densities in the range of $(0.5\text{-}1.4)\rho_c$, see the inset plot in Fig. 1a. Table 1 lists the running parameters performed in this paper.

Fig. 1c shows the simulation box with the three-dimensional sizes of $L_x{=}L_y{=}L_z$. Periodic boundary conditions are applied at all six surfaces of the simulation box. The simulation box contains 10976 atoms of argon for all the running cases. Based on Ref. [39,47], the number of particles of 10976 is sufficiently large to capture useful information for SFs. Because the calculations are performed at the critical temperature T_c, but the varied pressure for different running case yields the varied box size in a range from 29.0853σ to 40.9950σ, where σ is 3.405×10^{-10} m for argon. Simulations are conducted using LAMMPS [48], and Ovito software is used for atomic visualization.

The modified LJ potential is applied to consider the long-range interactions, which is written as [21,49]

$$\phi(r_{ij}) = \begin{cases} 4\varepsilon\left[(\sigma/r)^{12} - (\sigma/r)^6\right] + \phi_{TC} & (r < r_c) \\ 0 & (r > r_c) \end{cases} \tag{3}$$

where ϕ_{TC} is the tail correction defined as $\phi_{TC} = 2\pi\rho^* \int_{r_c}^{\infty} r^2 g(r)\phi(r)dr$ for the long-range interaction, where ρ^* is the number density, g (r) is the pair distribution function, and r_c is the cut-off radius, which is set as 5.8σ [50]. Table 2 lists the parameters of m, ε and σ for argon.

After energy minimization, the Velocity-Verlet algorithm is used to integrate the momentum equation. The timestep is set as 0.001τ, where τ is the characteristic time ($\tau = \sqrt{m\sigma^2/\varepsilon} = 2.16 \times 10^{-12}$ s). NVT and NPT ensembles are applied [51,52]. For the former, the volume of SB, the number of atoms and the temperature are kept to be constant. For the latter, the number of atoms, the pressure and the temperature are controlled. It is reported that for NPT ensemble, the volume of the SB may fluctuate, influencing the calculation accuracy of the local density [52]. Therefore, NVT ensemble is used instead of NPT ensemble. During calculation, fluid atoms are coupled with a thermostat of Nosé-Hoover [53,54], keeping the system temperature at $T{=}T_c$. The pressure is not a control parameter, but is determined by the temperature and density.

Fluid atoms are arranged as a face centered cubic (fcc) structure in the initial stage. For each running condition, a relaxation period exists before the system achieves equilibrium. Fig. 1d shows the variations of non-dimensional temperatures, pressures and energies versus time at the critical point after equilibrium, in which Pe is the potential energy. All the three curves reach equilibrium before 1000τ. During molecular dynamics simulations, the velocities need to be continuously corrected. Using temperature as an example, it is necessary to correct the velocity if the calculated temperature of system is too high or too low compared to the set temperature. The atomic velocity no longer requires correction when the temperature satisfies $0.9{\leq}T_{MD}/T_{set}{\leq}1.1$, where T_{MD} is the molecular dynamics results and T_{set} is the setting value. It is seen that the simulation and set values are in good agreement, and the temperature is well controlled to be at the set value. The size of the simulated box, the selection of the truncation radius and the statistical errors all contribute to the fluctuation of the statistical parameters [55]. Thus, noisy features are still present in the equilibrium stage beyond 1000τ. For all the running cases, the simulation time after equilibrium is $40000\ \tau$, which is sufficiently long for data analysis. For general consideration, the following non-dimensional parameters are applied including $x^* = \frac{x}{\sigma}$, $y^* = \frac{y}{\sigma}$, $z^* = \frac{z}{\sigma}$, $t^* = \frac{t}{\tau}$, $T^* = T\frac{k_B}{\varepsilon}$, $\rho^* = \frac{\rho\sigma^3}{m}$, $P^* = \frac{P\sigma^3}{\varepsilon}$.

3. Results and discussion

3.1. Density fluctuation and phase distribution

The investigation of critical phenomena of real fluid is more complex. Abnormal behavior of fluids approaching the critical point can be observed, appearing in the form of large-scale density fluctuations. Density fluctuation characteristics vary both in time and space. Some information will be lost when analyzing values that are averaged over a large space or over a long time. In order to obtain the spatiotemporal evolution characteristics of density fluctuations and conduct non-linear analysis on the density, we select the slice layer and the whole simulation system for density statistics, and analyze the evolution of density with time and space. The method of selecting the slice to observe the fluid structure has been applied in Ref. [39,56]. In many studies [39,50,57,58], large-scale and long-time (1~20 ns) MD simulations were performed for supercritical fluid to reproduce fluid thermophysical properties, structure,

Table 1
Summary of the simulation parameters.

Case	Temperature (k_BT/ε)	Non-dimensional density ($\rho^* = \rho\sigma^3/\varepsilon$)	Pressure ($P^* = P\sigma^3/\varepsilon$)
1	$T_c^* = k_BT_c/\varepsilon = 1.2458$	$0.5\rho_c^*{=}0.15939$	0.10572
2		$0.6\ \rho_c^*{=}0.19126$	0.11083
3		$0.7\ \rho_c^*{=}0.22314$	0.11360
4		$0.8\ \rho_c^*{=}0.25502$	0.11468
5		$0.9\ \rho_c^*{=}0.28689$	0.11494
6		$1.0\ \rho_c^*{=}0.31877$	0.11496
7		$1.1\ \rho_c^*{=}0.35065$	0.11497
8		$1.2\ \rho_c^*{=}0.38252$	0.11526
9		$1.3\ \rho_c^*{=}0.41440$	0.11677
10		$1.4\ \rho_c^*{=}0.44627$	0.12139

Table 2

. Parameters occurring in LJ potential.

working substance	atom mass m (kg)	energy parameter ε (J/K)	size parameter σ (m)
LJ fluid	6.63×10^{-26}	1.67×10^{-21}	3.405×10^{-10}

and density fluctuation. In this paper, we select 40000τ (~80 ns) production run to analyze the properties of fluid density fluctuation. The simulation time is several times longer than existing literature, ensuring the nonlinear analysis has enough data samples.

In order to perform transient and nonlinear analysis of local fluid density time series curves of different simulation conditions, in this paper, we choose the slice with a thickness of 3.45σ in the z direction, which is parallel to the xy plane, and obtain the statistical density in such a slice at each time, called local density. The nondimensional local density is

$$\rho\sigma^3 = \frac{\sigma^3}{A\Delta z(J_E - J_S + 1)} \sum_{J_S}^{J_E} N_{lo} \tag{4}$$

where J_S is the start time step and J_E is the end time step of the statistics, A is the xy plane area ($A=L_xL_y$), $\Delta z = 10\sigma$, N_{lo} is the total number of fluid molecules in the slice. N_{lo} changes over time, and the fluid local density of the slice varies with time, indicating the mass exchange between the slice and the nearby fluid domains. According to Eq.(4), the time series curves $X(t)$ of the local density in the slice are obtained.

Fig. 2 shows fluid densities in the slice bin with a 3.45σ thickness versus time, including five subfigures at different running conditions characterized by average density and pressure for each. These densities are oscillating with different amplitudes. Large amplitude oscillations are observed with the average densities of $0.8\rho_c$, $1.0\rho_c$, and $1.2\rho_c$. Attention is paid on the case with $\rho_{ave}=0.8\rho_c$, densities in the slice bin are larger than ρ_{ave} in the initial $20000\ \tau$ time period, indicating the collection process of atoms in the slice bin. Then, the densities gradually evolve to fluctuate around ρ_{ave}, indicating the breaking process of the atomic aggregation. For the cases of $0.5\rho_c$ and $1.4\rho_c$, oscillations of densities in the slice bin with small amplitudes and high frequencies are observed, display random feature of the oscillations. In one word, oscillations of local densities are different at different average densities and pressures.

Fig. 3 shows how densities in the slice bin deviate from the average densities at the critical temperature. Fig. 3a shows the probability density of local density time series (see Fig. 2). The vertical coordinate and horizontal coordinate refer to the probability density and the deviation degree of the local density with respect to the average density, respectively. The cases of $1.4\rho_c$ and $0.5\rho_c$ have the first and second largest probability for the local density being equal to the average density. These two cases also have the uniform distribution of the probability density curves against the zero deviation of the local density with respect to the average density. However, it is interesting to note the non-uniform distribution of the probability density curves for the cases of $0.8\ \rho_c$, $1.0\ \rho_c$ and $1.2\rho_c$. Fig. 3b further characteries the deviations of the local densities (ρ_{local}) in the slice bin from the average density (ρ_{ave}) in the whole simulation box. The root mean square error e_s characterizes the deviations of the local densities (ρ_{local}) in the slice from the average density (ρ_{ave}) in the whole simulation box. For local density time series of different working conditions (see Fig. 2), the relative error of each point is

$$e_i = \frac{\rho_{local} - \rho_{ave}}{\rho_{ave}} \tag{5}$$

The root mean square error e_s is expressed as

$$e_S = \sqrt{\frac{\sum_{i=1}^{N} e_i^2}{N}} \times 100\% \tag{6}$$

where N is the number of data points over series of time periods. In this paper, 40000τ data samples after the system equilibrium were chosen for deviation analysis. The deviation curve displays M-shape distribution, having lowest deviations at either lower average density of $0.5\rho_c$ or at the larger average density of $1.4\rho_c$. The M-shape curve have two peak points. It is interesting to observe the largest deviation taking place at $0.8\rho_c$, not at the exactly critical point of $1.0\rho_c$. Maddox et al. [59] explained that due to the non-ideality of LJ fluids, there is a short range potential effect, which will promote the system to form small physical clusters and cause density inhomogeneity, which is more significant at low density. One the other hand, the inhomogeneities are generated by critical fluctuations, which tend to be maximized at critical density. The competition between these two mechanisms causes the location of the maximum density fluctuations to occur below the critical density.

Pseudo-boiling was applied to explain the heat transfer of SF. Banuti developed the PB temperature for crossing the Widom line based on thermodynamic approach [60]. Xu et al. [61] determined two transition temperatures using MD simulations. Fig. 4 shows that SF can be divided into LL, TPL and GL, in which T_s is the transition temperature from LL to TPL, T_e is the transition temperature from TPL to GL. At the critical pressure ($P_r=P/P_c=1$), the density curve has two crossing points, marked as a and b, with the two transition boundaries of $\rho\sigma^3|_{T_s}$ and $\rho\sigma^3|_{T_e}$, determining GL, TPL and LL in the ranges of $\rho\sigma^3<0.154$, $0.154<\rho\sigma^3<0.495$, and $\rho\sigma^3>0.495$, respectively.

We note that Fig. 2 shows the time dependent densities in the slice bin (a local region), but Fig. 5 presents the non-dimensional densities over the xy plane but summarizes the whole height information of the simulation box. The presentation was performed at
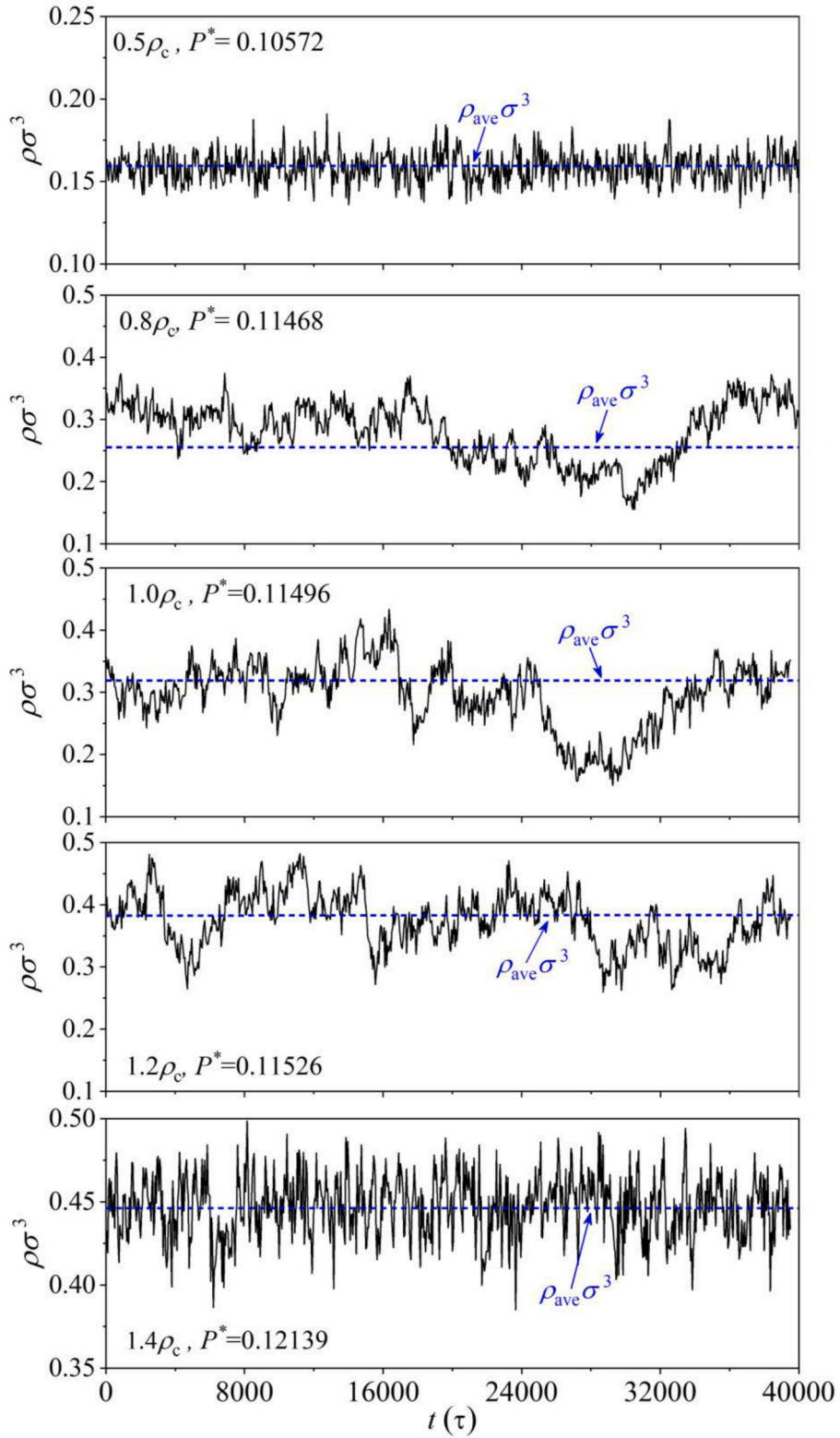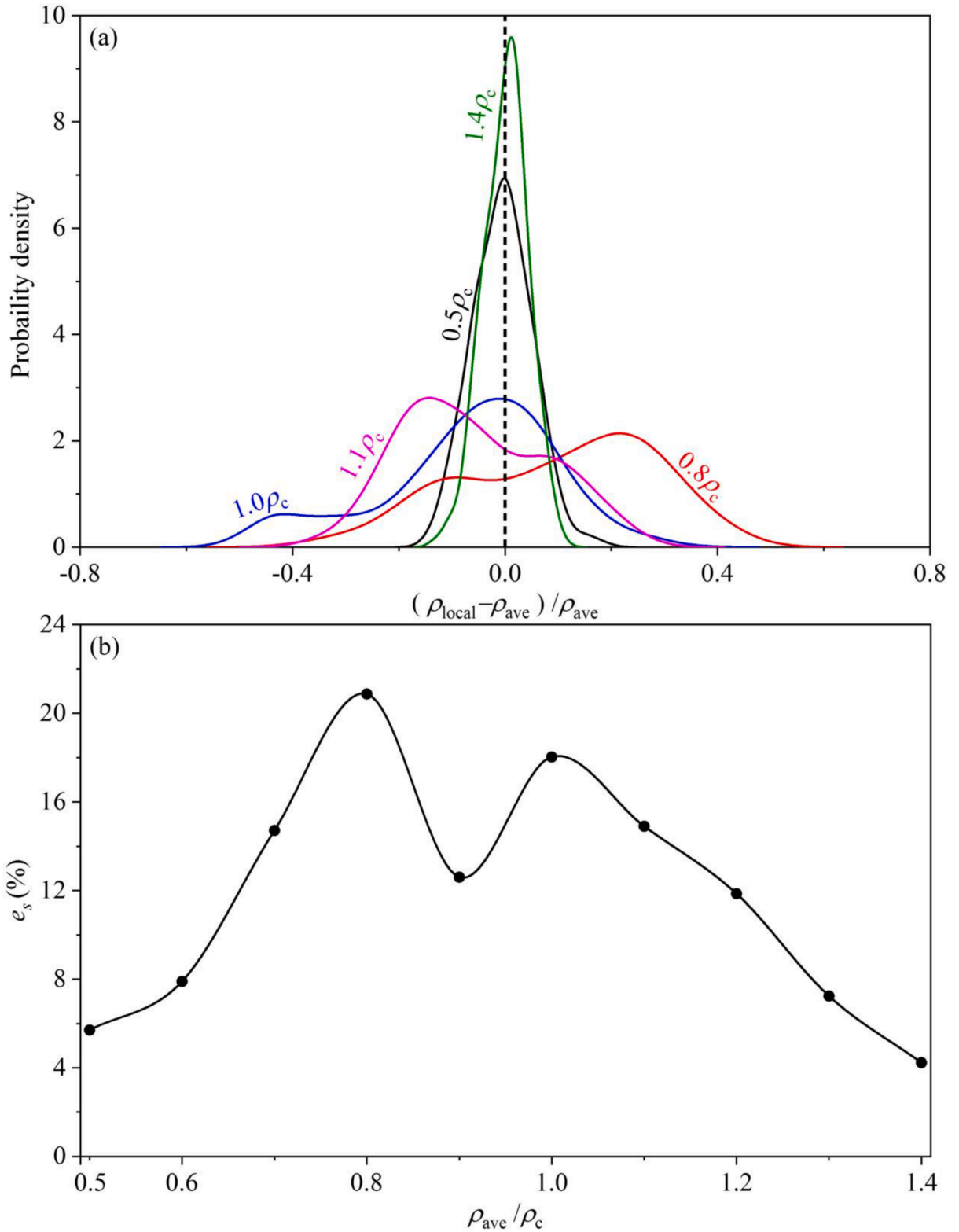
Fig. 2. Non-dimensional densities in the slice bin versus time at different running cases.

Fig. 3. Deviation of the density in the slice bin from the average density in the simulation box. (a) the probability density with respect to the density deviation, (b) the square root error (deviation) influenced by average densities.
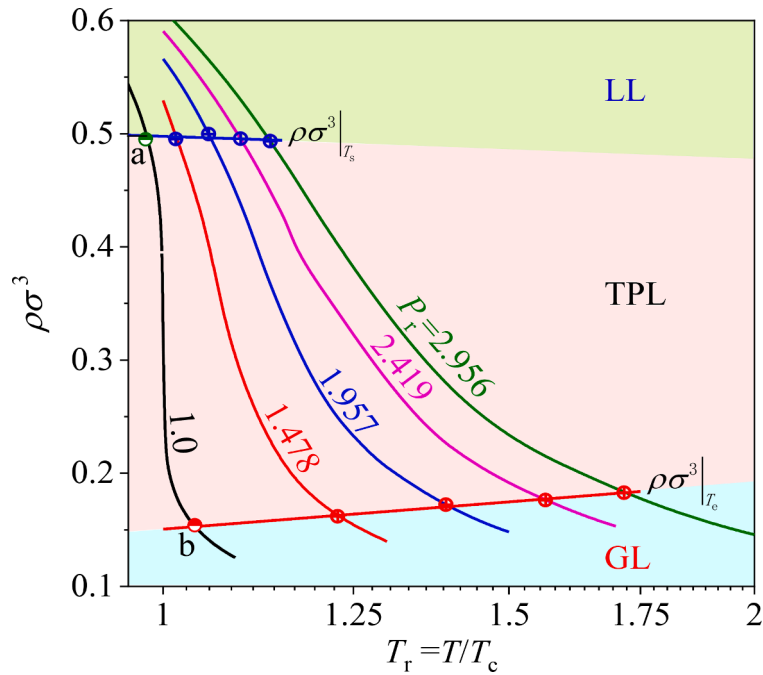
Fig. 4. The transition boundaries among the three regimes of GL, TPL and LL. The data are recalculated based on the method reported in [61] and the figure is replotted based on [61].

the critical pressure and temperature, for which red spot and blue spot represent densely populated particles and sparsely populated particles, respectively. Hence, the former indicates the liquid-like behavior but the latter represents the gas-like behavior. Fig. 5 shows the density distribution of the simulated box on the *xy* plane at the critical operating condition, showing 6 states in the time range of 16350τ-17200τ. The non-uniform distribution of density confirms the heterogeneous characteristic of supercritical argon. It can be seen that the size, position and shape of the three regimes all vary over time and space. Both LL and GL regions have experienced an evolution process containing formation, destruction, and reconstruction. Such phase distribution on the *xy* plane also varied over time, and different phase distribution states are obtained when the statistical time is changed. In summary, Fig. 2 indicates the time dependent behavior of the local densities, and Fig. 5 indicates the time dependent phase distribution over the whole simulation box.

The study of heterogeneous fluids requires techniques that typically identify and classify fluid properties based on the number of neighbors near a molecule [62,63]. In the simulation box, each molecule can be selected as a target molecule. For a sphere having 1.5σ radius with this target molecule, the number of molecules is counted excluding the target molecule, which is called the number of neighboring molecules. The probability curves were plotted for different average densities of the system, displaying parabola distribution with a peak point for each curve. We recall that if a target molecule has more than four neighboring molecules, the target molecule is named as a liquid-like molecule. Alternatively, the target molecule is called a gas-like molecule [64–66]. This method has good applicability for analyzing the inhomogeneity of SF and has been recommended by Xu and Wang [61] and Losey and Sadus [65], and it is also used here. Fig. 6 characterizes the non-uniform distribution of the molecules in the simulation box, plotted based on the neighboring molecules method. In this paper, 40000τ data samples after the system reaching equilibrium were chosen for heterogeneity analysis. The probability curves were plotted for different average densities of the system, displaying parabola distribution with a peak point for each curve. We recall that if a target molecule has more than four neighboring molecules, the target molecule is named as a liquid-like molecule. Alternatively, the target molecule is called a gas-like molecule [64,65]. The probability curve has a wide range of the number of neighboring molecules, indicating that the system contains the mixture of liquid-like molecules and gas-like molecules. It is observed that with increase of the average density, the peak point shifts toward right with larger number of neighboring molecules. We further count the number of clusters in the system.

The structural mechanism explains the inhomogeneous distribution of molecules [59], which is also called the potential induced mechanism [37]. Fig. 7a-b plots non-dimensional potential (ϕ/ε) and non-dimensional force ($F\sigma/\varepsilon$) versus the distance between two molecules (*r*). Repulsive forces exist for $r<1.12\sigma$, beyond which attractive forces exist. In order to qualitatively analyze the impact of potential energy on density fluctuations, the average distance between molecules under each density is obtained by assuming a uniform distribution of molecules within the simulation box. The average distance determines the strength of interatomic interactions in the simulation box and thus determines density fluctuations. In this paper, the representative working conditions of high, medium and low densities are chosen for qualitatively analysis. Three points are marked as a, b and c in Fig. 7b, representing dense population, moderate population, and sparse population of molecules. For dense population with small *r*, attractive force is large to confine many particles at their equilibrium positions, approaching uniform distribution of molecules. This situation displays liquid-like behavior. In another extreme of sparse distribution with large *r*, attractive force is very small and approaches zero, and molecules can move freely
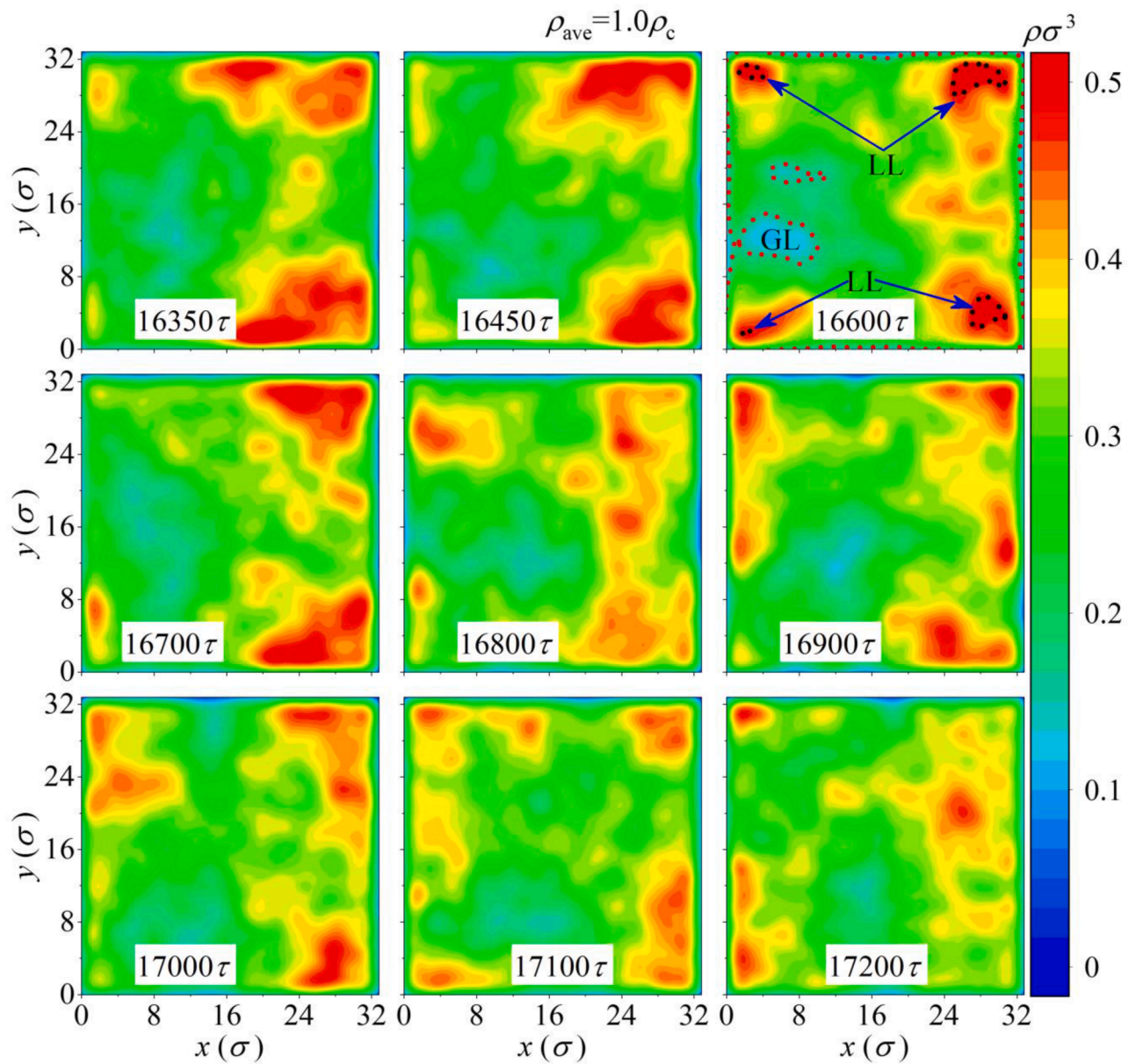
Fig. 5. Phase distribution on the *xy* plane summarizing the information in the whole height of the simulation box at the critical point of P_c and T_c.
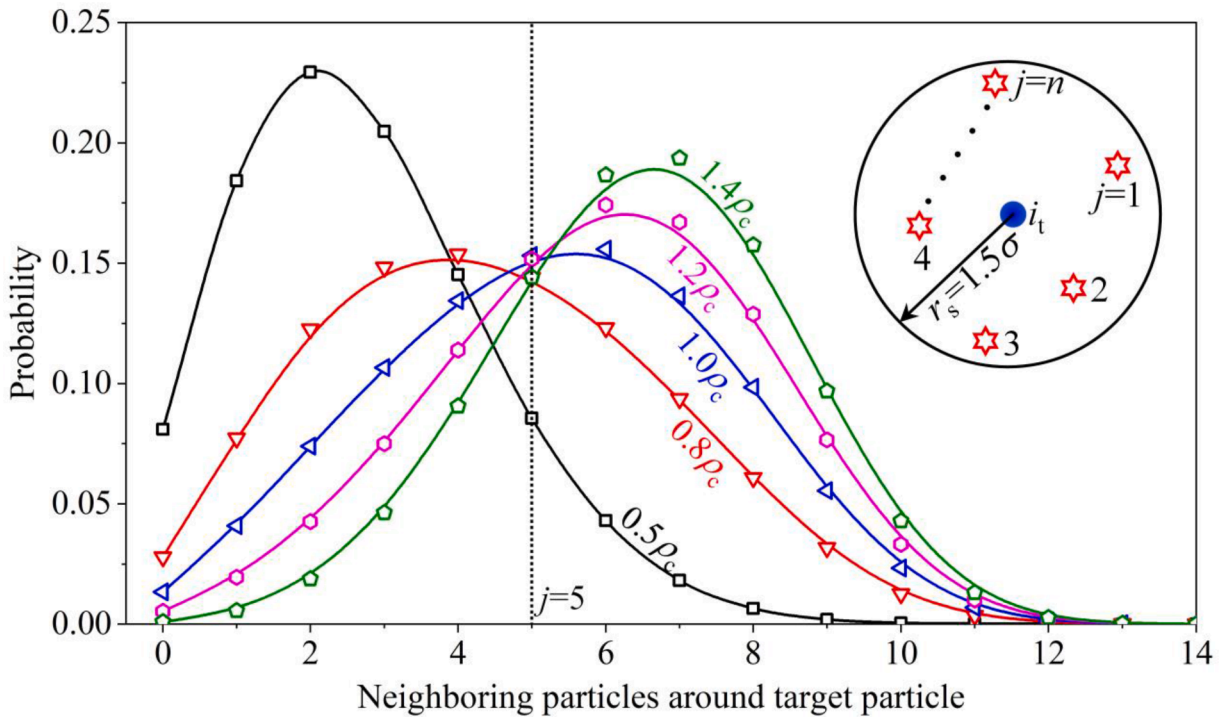
Fig. 6. Characterization of the non-uniformity distribution of molecules in the simulation box, the probability distribution of neighboring particles per target particle.

and have strong homogeneity. This situation corresponds to gas-like behavior. However, if r is moderate, the force varies gently with r. Some molecules decrease their distance to form clusters of molecules, but some molecules increase their distance to form voids in the fluid. The density fluctuation and phase distribution corresponding to the three points are shown in Fig. 7c. This mechanism qualitatively explains the phenomenon of strong density fluctuations near the critical point, presenting a mixture of liquid-like and gas-like.

The critical fluctuation can also explain the heterogeneous characteristic of molecules. Based on statistical mechanics, there are molecular aggregation and vacancy in molecules system. Density fluctuations produce microscopic inhomogeneity. Fluctuations at one spatial location are related to those at other spatial location [67]. Correlation length characterizes the correlated region size [68]

$$\xi(P)\propto|P-P_{\mathrm{c}}|^{-\gamma} \tag{7}$$

where the exponent γ is 0.8-0.9 in a three-dimensional system [68]. For the pressure approaching the critical pressure at the critical temperature T_{c}, the correlation length $\xi(P)$ attains maximum (see Fig. 8). Practically, $\xi(P)$ reaches infinite at the critical point [37]. When the fluid deviates from the critical point, the correlation length rapidly decreases, but it is still much greater than the intermolecular interaction distance. Thus, the critical fluctuation belongs to long-range effect. The isothermal compression coefficient κ_{T} is directly related to the density fluctuation. The density fluctuation can be calculated based on isothermal compression coefficient κ_{T} as [68]

$$\frac{\langle(\Delta N)^2\rangle}{\langle N\rangle} = \rho_{\mathrm{ave}}\kappa_{\mathrm{T}}k_{\mathrm{B}}T \tag{8}$$

Nichele et al [69] used MD simulation to calculate κ_{T} of LJ fluid near the critical point, agreeing with the NIST data. The maximum deviation between MD simulations and NIST data is smaller than 15%. Hence, we use κ_{T} calculated by the NIST software to perform the analysis since κ_{T} is an easily obtainable parameter. Fig. 8 plots κ_{T} versus non-dimensional average densities. Because density fluctuation is proportional to κ_{T} (see Eq.8), at the critical point, κ_{T} reaches the maximum value, corresponding to the largest density fluctuation amplitude.

In summary, the heterogeneous structure of SF can be attributed to the potential induced mechanism and the critical fluctuation mechanism. The potential induced mechanism is effective over the full phase diagram, while the critical fluctuation mechanism is only effective near critical point. At low average density away from the critical density, the potential induced effect dominates. As the density increases and approaches the critical density, the effect from the critical fluctuation mechanism gradually becomes significant, and both mechanisms play important roles. Under the combined action of the two mechanisms, the strongest heterogeneity appears not at the critical point, but below the critical point at $\rho_{\mathrm{ave}}=0.8\rho_{\mathrm{c}}$, which is consistent with Ref. [70].
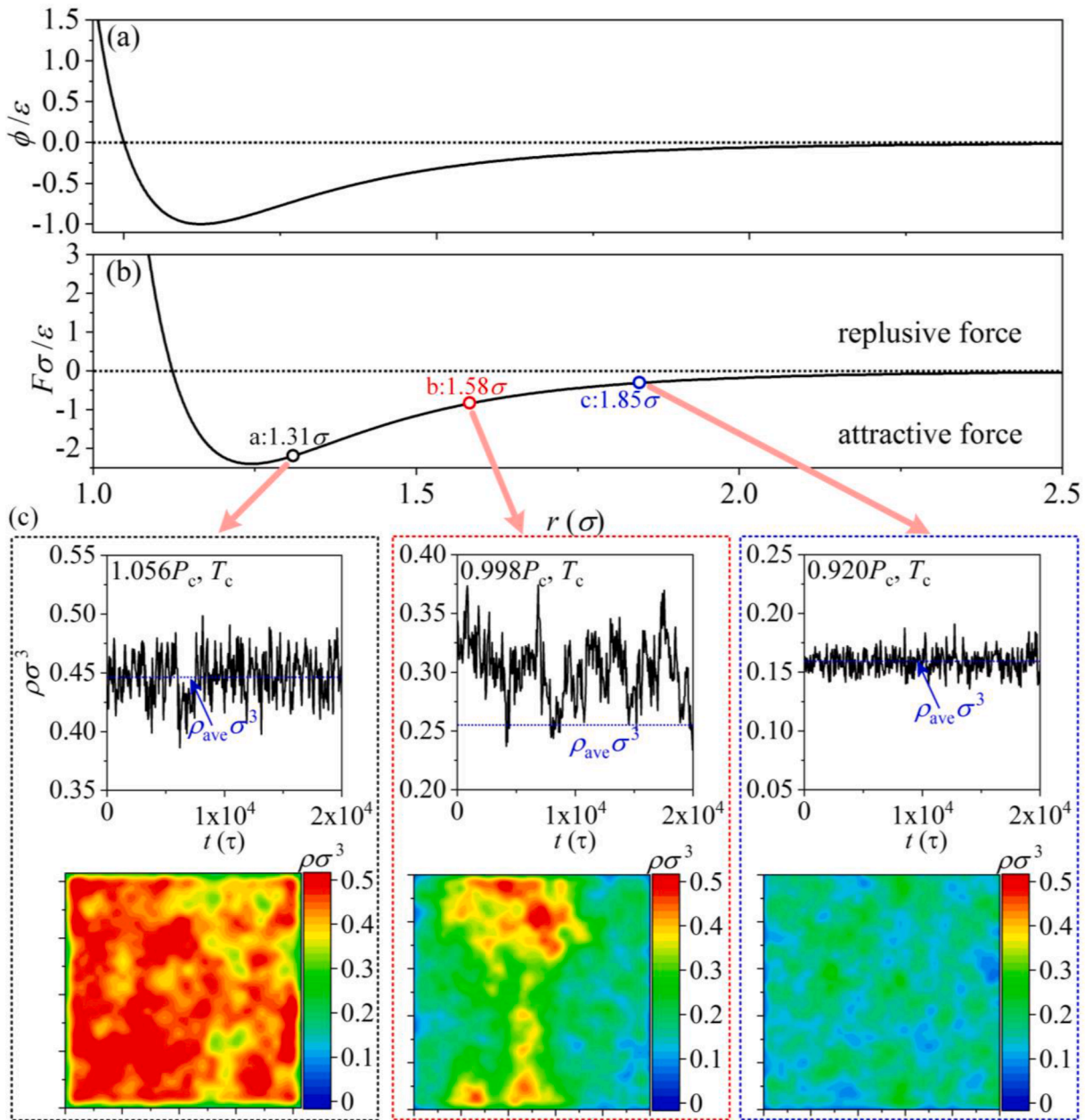
Fig. 7. Uniformity degree of molecules explained by the potential induced mechanism. (a) non-dimensional potential versus *r*; (b) non-dimensional forces versus *r*; (c) density fluctuations and phase distribution corresponding to three different conditions.

3.2. Nonlinear analysis

3.2.1. Why do we need nonlinear analysis for SF?

Classically, supercritical fluid (SF) is regarded as single-phase fluid without bubbles and related interface [13]. In SF, a thermodynamic parameter such as density is solely determined based on the state parameters of pressure and temperature. However, we demonstrate oscillations of local densities in the slice bin, and two-phase-like feature of SF. To further identify the two-phase-like feature of SF and how the complicated SF system evolves versus time, the chaotic analysis is introduced. The chaotic analysis is not necessary for single-phase system due to weak nonlinear effect. The system is completely predictable. However, multiphase system is a strong nonlinear system, due to the complicated interactions of mass, momentum, and energy between liquid and gas. In a multiphase system, it seems that many parameters such as densities and pressures oscillate irregularly, the purpose of nonlinear analysis is summarized as: (1) identify a system being chaotic or random. A chaotic system is partially predictable, but a random system is
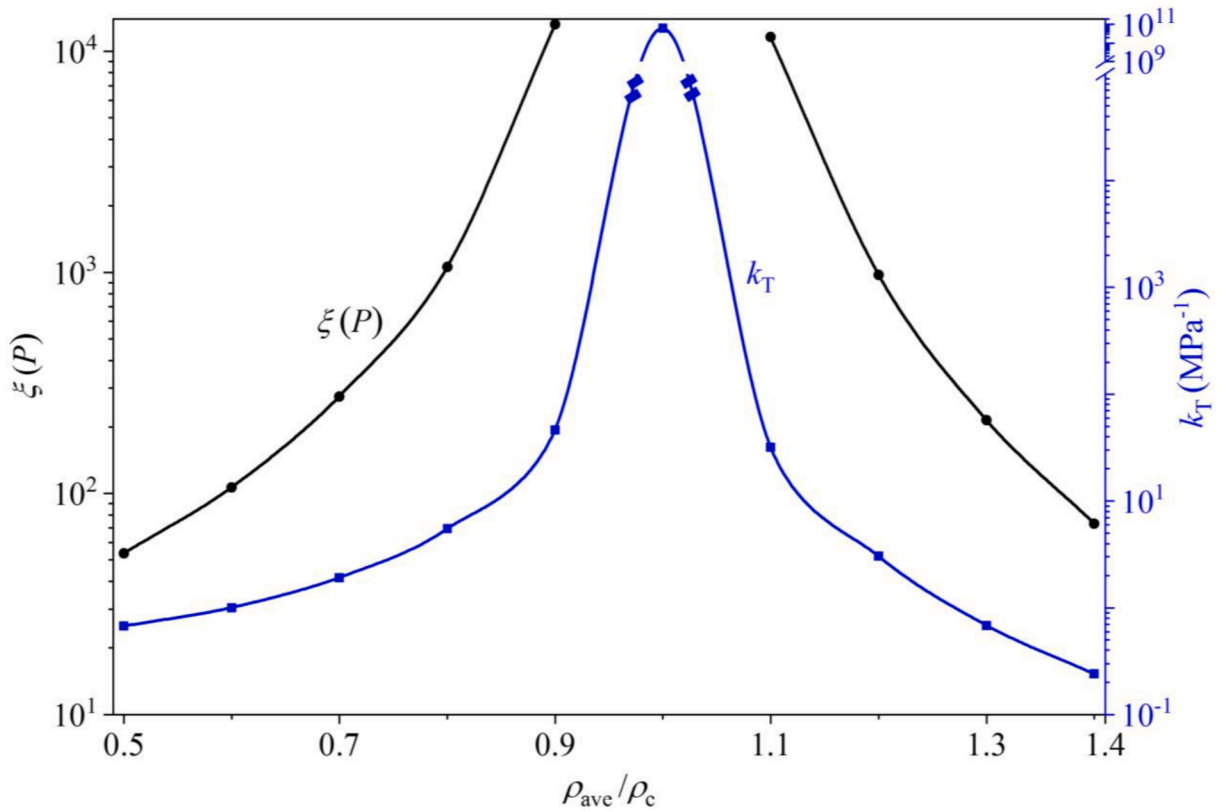
Fig. 8. Correlation length and isothermal compressibility coefficient versus average densities at the critical temperature T_c.

completely non-predictable. (2) establish the phase space to see the internal structural of the attractor. The attractor is completely irregular for random system, has regular structure for chaotic system. (3) understand how complex a nonlinear system is. The correlation dimension determines the minimum number of parameters that is necessary to describe the system. The larger the number is, the more complex the system is.

3.2.2. Approaches of the nonlinear analysis

In this paper, we use the nonlinear analysis. The input data come from the time series signal. Here, the time series densities in the slice bin are the input data (see Fig. 2). The autocorrelation function, reconstruction of phase space and correlation dimensions are calculated.

3.2.2.1. Autocorrelation function (ACF). Earlier in this paper, we obtained the time series $X(t)$ of local density in the slice. *ACF* represents the relationship of a parameter such as local density $\rho\sigma^3$ at different time steps, i.e., the degree of correlation between different instantaneous values. *ACF* is

$$ACF(\tau_D) = \frac{\int\limits_{t=1}^{N-\tau_D} [X(t)][X(t+\tau_D)]dt}{\int\limits_{t=1}^{N} [X(t)]^2 dt} \tag{9}$$

where τ_D is the delay time, N is the total number of data. For periodic time series, *ACF* displays periodic feature. For random signal, *ACF* quickly decays to zero as soon as time increases, representing the parameters not related at different time steps. For chaotic system, *ACF* gradually approaches zero, representing partially related of parameters at different time steps.

3.2.2.2. Reconstruction of phase space. The phase diagram is the trajectory displayed by the attractor in the phase space, showing the geometric structure of the attractor. For the univariate time series obtained by the simulation, multidimensional attractors can be obtained by reconstructing the phase space. At present, the delayed coordinate phase space reconstruction method is widely used, and the delay time τ_D can be obtained according to the *ACF*. The multidimensional phase space portraits can be reconstructed from the time

series of density fluctuations [71], the same method described in Ref. [42]. From the MD simulations, the time series density signal $X(t)$ is obtained. The vector time series X_v is defined as [52]

$$X_v = \{X(t), X(t+\tau_D), X(t+2\tau_D), \ldots X(t+(n-1)\tau_D\}$$ (10)

where n is the embedding dimension and τ_D is the time delay, which is determined based on *ACF*.

3.2.2.3. Correlation dimension. The correlation dimension reflects the degree of freedom of the system, and indicates the minimum number of independent variables to determine the system dynamics, which is an important parameter for chaotic quantitative analysis. The correlation dimension D_2 can be determined by the power-law relationship between correlation integration of attractors and the neighborhood radius of the analysis hypersphere [61,72] as

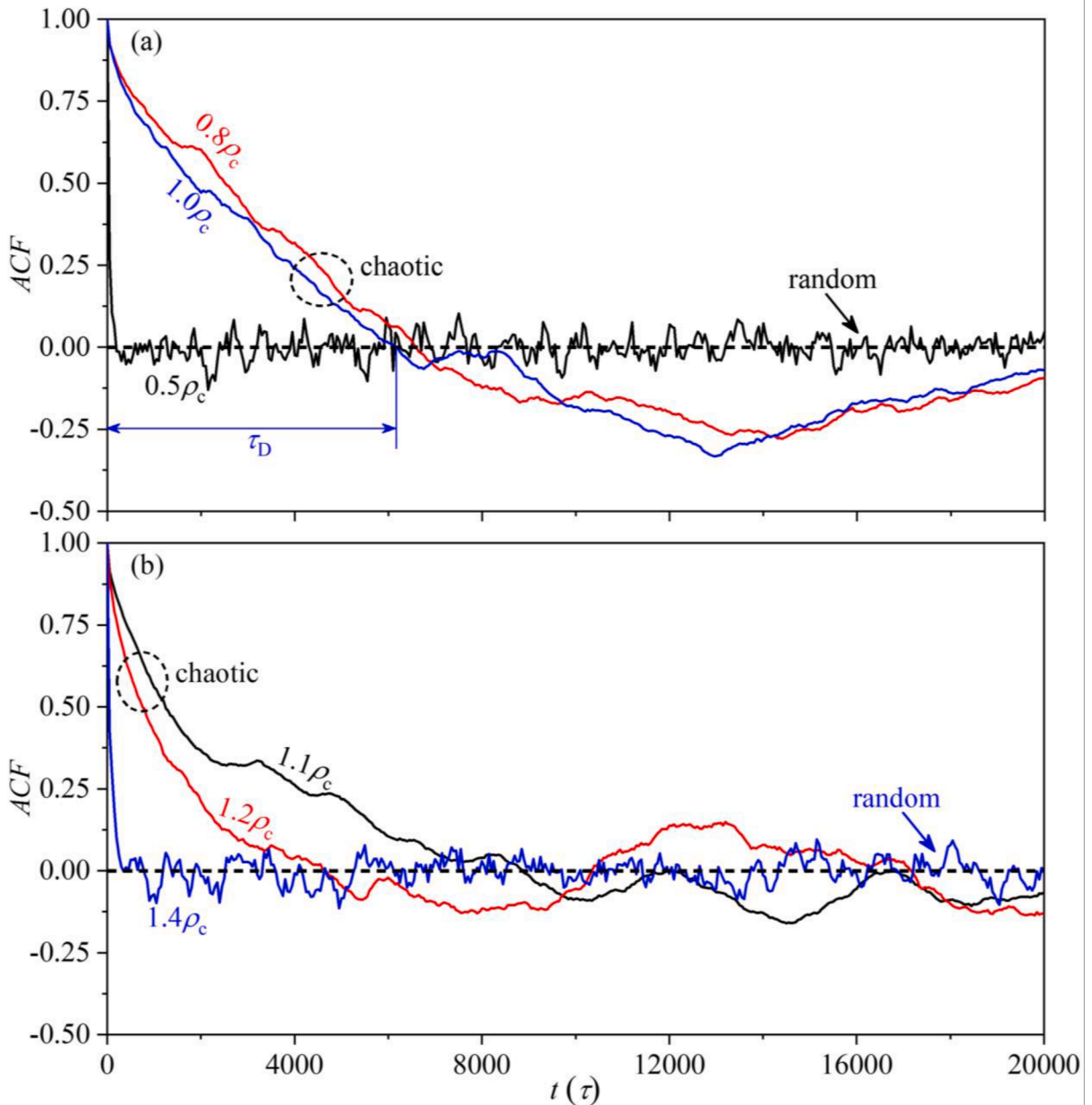$$D_2 = \lim_{r \to 0} \frac{\ln C(r_d)}{\ln r_d}$$ (11)

Fig. 9. Autocorrelation function based on time series of densities in the slice bin. (a) $0.5\rho_c$, $0.8\rho_c$ and $1.0\rho_c$; (b) $1.1\rho_c$, $1.2\rho_c$ and $1.4\rho_c$.
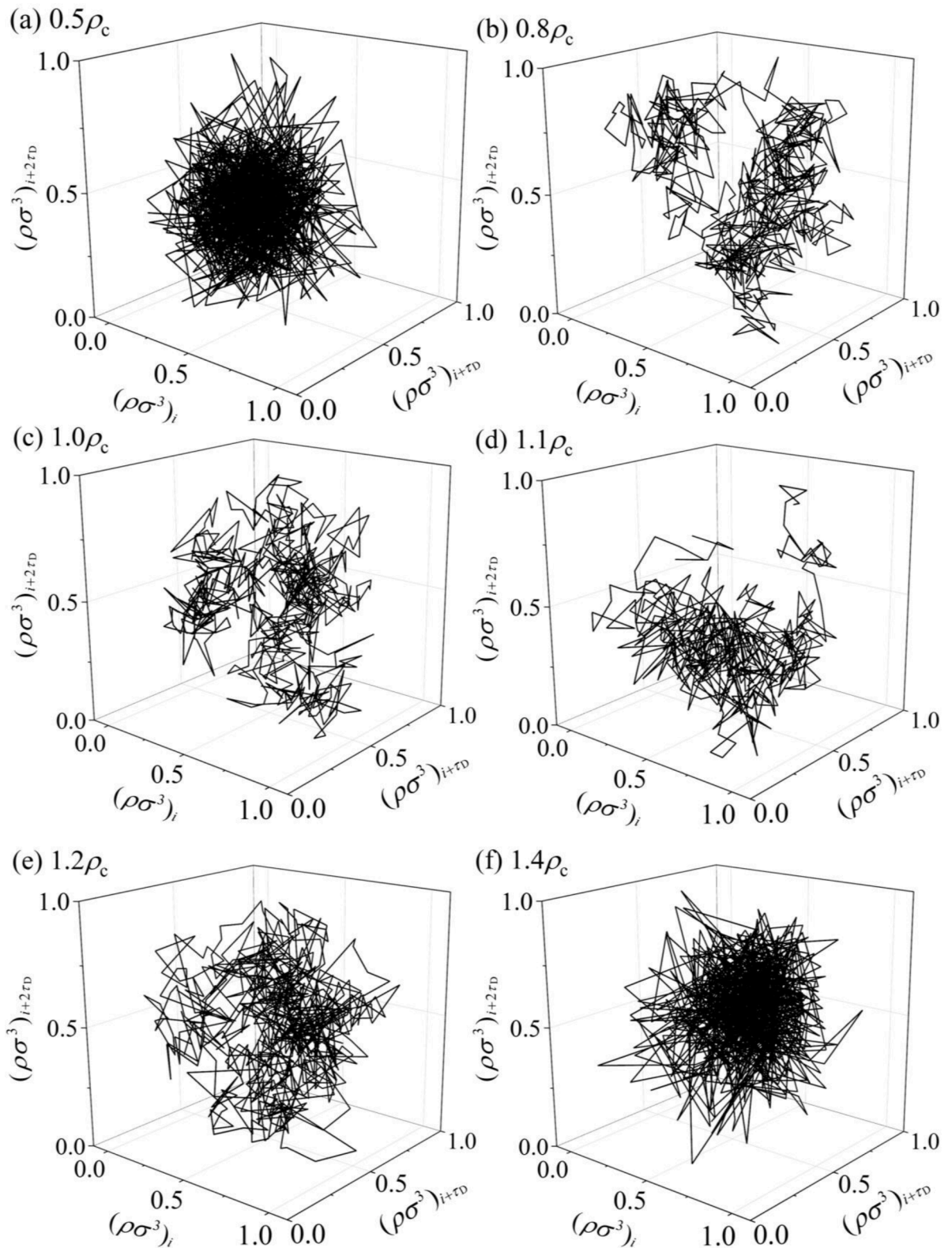
Fig. 10. Structure of phase space (attractor). (a) and (f) are for random system, (b-e) are for chaotic system.
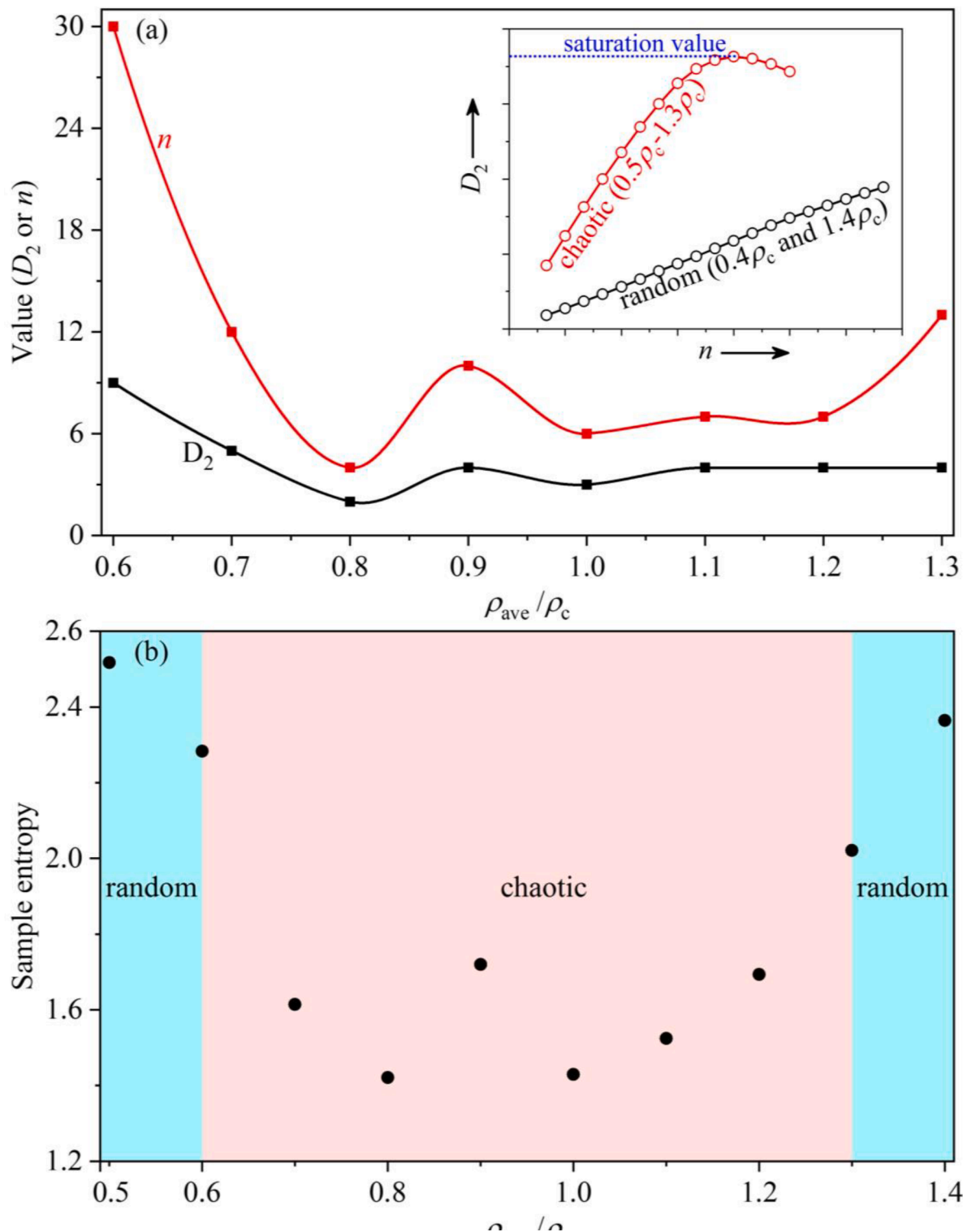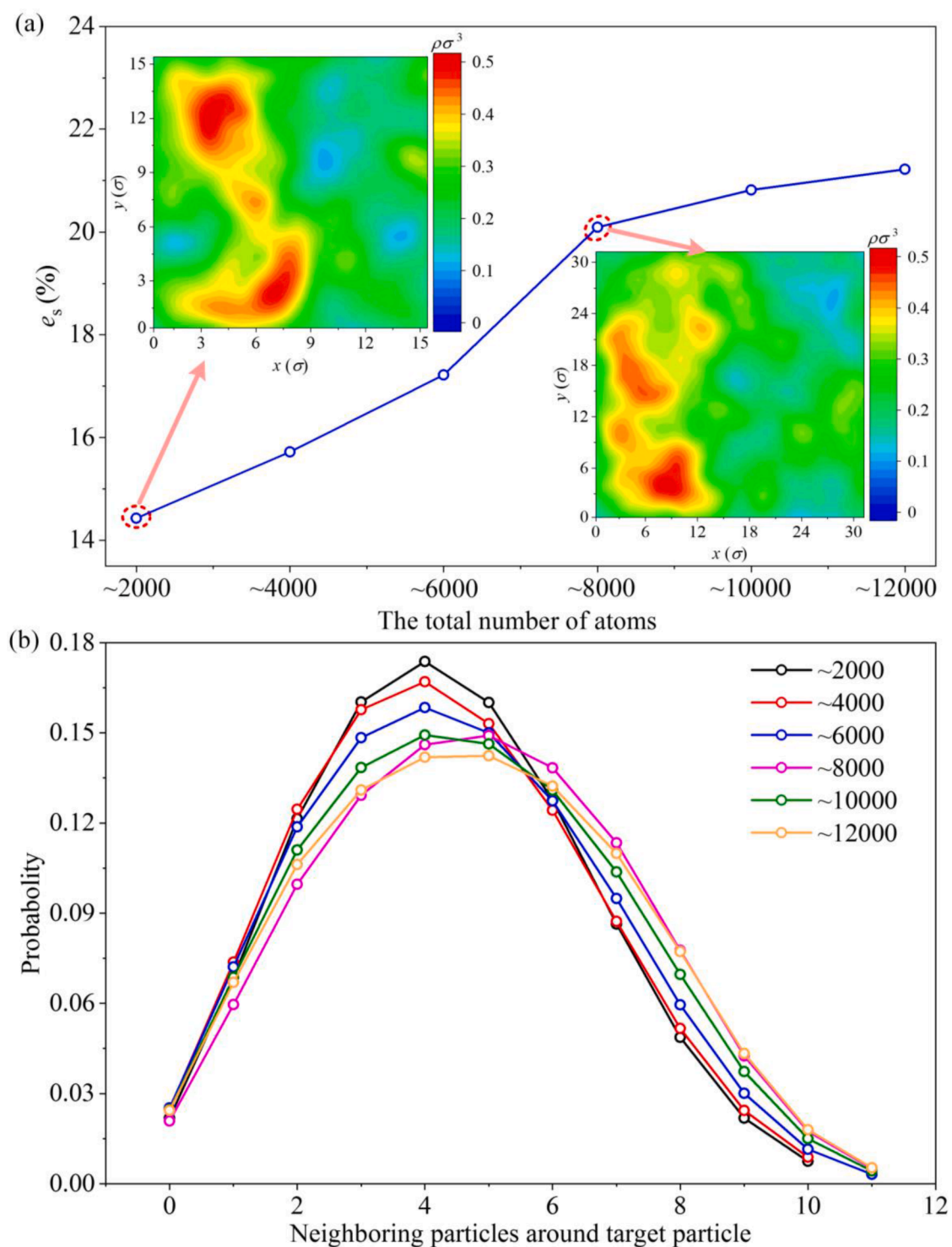
Fig. 11. The degree of complex of LJ fluid. (a) correlation dimensions at various average densities, (b) sample entropies at various average densities.

Fig. 12. Size effect on system performance. (a) the size effect on the deviations of local density from average density; (b) the size effect on the probability of neighboring molecules for target molecule.

where $C(r_d)$ is the correlation integral defined by $C(r_d) = \frac{2}{N_d(N_d-1)} \sum_{j=1}^{N_d} \sum_{i=j+1}^{N_d} \theta(r_d - |\vec{x}_i - \vec{x}_j|)$, in which x_i is the points on the attractor and N_d is the number of embedding points in phase space. $\theta(\bullet)$ is the Heaviside step function, which is defined as

$$\theta(x) = \begin{cases} 0, & x \leq 0 \\ 1, & x > 0 \end{cases} \tag{12}$$

3.2.3. Outcomes of the nonlinear analysis of SF

It is assumed that there is a linear relationship between time series data points, and the autocorrelation function (ACF) expresses the degree of linear correlation between different steps in local density time series. The ACF of periodic signals is also periodic, the ACF of chaotic signals gradually tends to zero, and the ACF of random signals is close to zero as soon as time increases. Fig. 9 presents ACF with ρ_{ave} from $0.5\rho_c$ to $1.4\rho_c$. At the two extreme average densities of $0.5\rho_c$ and $1.4\rho_c$, ACF sharply drops to zero, indicating the system to be random and not predictable. With $\rho_{ave}=0.8\rho_c$, $1.0\rho_c$, $1.1\rho_c$ and $1.2\rho_c$, ACF slowly decreases, reaches zero at a relaxation time τ_D, and then oscillates, indicating the system to be chaotic. The τ_D will be used for the construction of phase space (attractor) and correlation dimension.

Attractor reconstruction was carried out using the method described in Section 3.2.2. Two types of attractor patterns were identified for the different simulation conditions of this work, as shown in Fig. 10. Conditions with $\rho_{ave}=0.5\rho_c$ and $1.4\rho_c$ show the type-I attractor, having numerous irregular lines in the phase space, which makes it difficult to observe the internal structure of the attractor, and the attractor converges toward the center (see Fig. 10a and f). The disorder and irregularity of the attractor structure indicate random behavior. On the other hand, the type-II attractor is shown in Fig. 10b~e (with $\rho_{ave}=0.8\rho_c$, $1.0\rho_c$, $1.1\rho_c$ and $1.2\rho_c$). The attractor pattern is densely populated in some local phase spaces but is very sparse in other regions. The attractor pattern is composed of superimposed multiphase loops and has a fine internal structure, corresponding to chaotic behavior of the time series density signal. This feature is very similar to the two-phase system in subcritical pressure.

Correlation dimension (D_2) and embedding dimension (n) represent minimum number and maximum number of independent parameters to describe the system. Thus, the two parameters characterize the complex degree of the system. The D_2 and n are plotted versus average densities in Fig. 11a. We note that the two parameters are not presented for $0.5\rho_c$ and $1.4\rho_c$. For random system, with increase of embedding dimensions, correlation dimensions do not have a saturation value and diverge (see the inset-figure in Fig. 11a). Fig. 11a indicates that the system is more complex with $0.6\rho_c$ than those with other average densities. The most complex condition does not take place at the exactly critical point.

In 1991, Pincus applied the notion of "entropy" to the real world [73]. Entropy means the order or complexity or regularity. The idea is that time series from more ordered systems with repeating elements have smaller entropy values. If the data set is infinite and perfect, it would be possible to determine an exact entropy value. For data set that is finite or imperfect, Pincus introduced the approximate entropy [73], which is simple but has practical issues in implementing the algorithm. These motivated Richman et al. [74] to develop new sample entropy as an alternative method to entropy estimation for real word data [74]. The calculation method of sample entropy is as follows:

(1) The signal X is a time series of length N_r, $X=[x(1), X(2), …, X(N_r)]$. Convert time series X to matrix X_n, $X_n(i)=[x(i), X(i+1), …, X(i+n-1)]$, $i=1,2,…,N_r-n+1$, n is the embedding dimension.
(2) Define the distance d_{ij} between two vectors as $d_{ij} = \max(|x(i+k) - x(j+k)|, k = 0, 1, ..., n-1, i \neq j)$
(3) Calculate the ratio $B_i^n(r_e) = num(d_{ij} < r_e)/(N_r - n)$, where $1 \leq j \leq N_r-n$; $j \neq i$, and $B^n(r_e) = \frac{1}{N_r-n+1} \sum_{i=1}^{N_r-n+1} B_i^n(r_e)$.
(4) Let $n=n+1$, repeat the above steps, and obtain $B^{n+1}(r_e)$. The sample entropy $SE(n, r_e)$ can be finally obtained as $SE(n, r_e) = -\ln[B^{n+1}(r_e)/B^n(r_e)]$.

During the calculation, $n=2$. The value range of r_e is $(0.1~0.25)Std$, where Std is the standard deviation of time series. This method is recommended by Zurek et al. [75] and Pham et al. [76], and is also used here. From the above method, we identify that the system is either random or chaotic. The random system has a strong degree of chaos, showing a large sample entropy. For a chaotic system, the system has a low degree of chaos, the local ordered structure exits, and the sample entropy is small. Fig. 11b presents the sample entropies at different average densities. The sample entropies are much higher for $\rho_{ave}<0.6\rho_c$ and $\rho_{ave}>1.3\rho_c$, indicating more disordered characteristic of the system under such conditions. The non-linear dynamics proves that SF in random state displays more disordered degree than that in chaotic state.

Previous MD simulations show snapshoot pictures to demonstrate inhomogeneous molecules for SF [39–41]. In this paper, we found that with the average densities in the range from $0.5\rho_c$ to $1.4\rho_c$ at the critical temperature, local densities in the slice bin oscillate versus time irregularly. Most importantly, the phase distribution contains the mixture of liquid islands and vapor voids. Inspired by the two-phase-like characteristic of SF, nonlinear analysis is introduced for the analysis of the complicated system. Our results indicated that SF is either random or chaotic, depending on the average densities. The chaotic SF is partially predictable, but the random SF is not predictable. The degree of complex for SF is characterized by the autocorrelation function and the correlation dimension. Random SF has irregular pattern of attractors, but internal structure can be observed for chaotic SF. Random SF displays more disordered feature than chaotic SF.

We note that the above outcomes come from the simulations using 10976 molecules in the simulation box, which is sufficiently large to acquire useful information. The size effect on system performance is performed with the number of molecules in the simulation box varied from ~2,000 to ~12,000. For any size in this range, the system behavior is similar, qualitatively. The spatial-temporal molecules display liquid-like, two-phase-like, or gas-like, depending on average densities. SF is either random for liquid-like and gas-like, or chaotic for two-phase-like. Fig. 12 quantifies effect of the number of molecules in the simulation box on system performance. The deviation of local density in the slice bin from the average density, characterized by square root error (e_s), increases with increase of the simulated particle number. The curve slope decreases for larger particles system, i.e., the increase speed of e_s decreases with increase of particles number (see Fig. 12a). The probability versus the number of neighboring molecules for target molecule is plotted in Fig. 12b, displaying parabola shape. The peak value takes place at the four neighboring molecules for target molecule. The probability at the peak point is larger for smaller molecules system, and decreases for larger particles system. The decrease speed of the peak probability decreases with increase of the number of simulation particles. Fig. 12 concludes the sensitivity of the simulation box size becomes weak when the molecules number is larger than 10^4.

4. Conclusions

MD simulations of supercritical fluid are performed at the critical temperature but with varied average densities in a range of $0.5\rho_c$ ~$1.4\rho_c$. Conclusions are summarized as follows.

(1) High-frequency/low-amplitude density oscillations in the slice bin exist at $0.5\rho_c$ and $1.4\rho_c$, but low-frequency/high amplitude oscillations exist with ρ_{ave} from $0.6\rho_c$ to $1.3\rho_c$. The maximum deviation of local densities from average density occurs at $0.8\rho_c$ instead of ρ_c at the exactly critical point.
(2) Transition boundaries among three regimes of liquid-like, two-phase-like and gas-like are determined. Two-phase-like is observed to contain liquid islands and vapor voids. Phase distribution evolves versus time. Local density oscillation and phase distribution are explained by potential induced and critical fluctuation mechanisms.
(3) Nonlinear analysis is introduced to analyze the complicated SF, which is either random or chaotic, depending on average densities. The chaotic SF is partially predictable, but the random SF is not predictable. The degree of complex for SF is characterized by autocorrelation function and correlation dimension. Random SF has irregular attractors, but internal structure of attractors can be seen for chaotic SF.
(4) SF displays similar behavior with the number of molecules varied from ~2,000 to ~12,000. The deviation of local density from average density increases with increase of the box size, but the slope becomes decreased for larger particles system. The probability peak takes place for four neighboring molecules for target molecule, but the peak amplitude decreases for larger particles system. The ~10^4 particles in the simulation box is sufficient to acquire useful information.

Declaration of Competing Interest

The authors declare that they have no known competing financial interests or personal relationships that could have appeared to influence the work reported in this paper.

Acknowledgments

References

[1] B. Subramaniam, R.V Chaudhari, A.S. Chaudhari, G.R. Akien, Z. Xie, Supercritical fluids and gas-expanded liquids as tunable media for multiphase catalytic reactions, Chem. Eng. Sci. 115 (2014) 3–18.
[2] K.P. Johnston, P.S. Shah, Making nanoscale materials with supercritical fluids, Science 303 (2004) 482–483.
[3] J. Xu, E. Sun, M. Li, H. Liu, B. Zhu, Key issues and solution strategies for supercritical carbon dioxide coal fired power plant, Energy 157 (2018) 227–246.
[4] W.H. Stein, R. Buck, Advanced power cycles for concentrated solar power, Sol. Energy 152 (2017) 91–105.
[5] L. Guo, H. Jin, Y. Lu, Supercritical water gasification research and development in China, J. Supercrit. Fluid. 96 (2015) 144–150.
[6] H. Pińkowska, P. Wolak, A. Złocińska, Hydrothermal decomposition of alkali lignin in sub-and supercritical water, Chem. Eng. J. 187 (2012) 410–414.
[7] F. Van Rantwijk, R.A. Sheldon, Biocatalysis in ionic liquids, Chem. Rev. 107 (2007) 2757–2785.
[8] L. Qian, S. Wang, D. Xu, Y. Guo, X. Tang, L. Wang, Treatment of municipal sewage sludge in supercritical water: a review, Water Res. 89 (2016) 118–131.
[9] I.N. Levine, Physical Chemistry, (Ed. 6), Thomas Timp, 2002.
[10] J. Zhang, A.H. Markosyan, M. Seeger, E.M. van Veldhuizen, E.J.M. Van Heesch, U. Ebert, Numerical and experimental investigation of dielectric recovery in supercritical N_2, Plasma Sources Sci. T. 24 (2015), 25008.
[11] J. Zhang, E.J.M. van Heesch, F. Beckers, A.J.M. Pemen, R.P.P. Smeets, T. Namihira, A.H. Markosyan, Breakdown strength and dielectric recovery in a high pressure supercritical nitrogen switch, IEEE T. Dielect. El. In. 22 (2015) 1823–1832.
[12] P.G. Debenedetti, Supercooled and glassy water, J. Phys. Condens. Mat. 15 (2003), R1669.
[13] Y.A. Cengel, M.A. Boles, M. Kanoglu, Thermodynamics: An Engineering Approach, McGraw-hill New York, 2011.
[14] G.G. Simeoni, T. Bryk, F.A. Gorelli, M. Krisch, G. Ruocco, M. Santoro, T. Scopigno, The Widom line as the crossover between liquid-like and gas-like behaviour in supercritical fluids, Nat. Phys. 6 (2010) 503–507.
[15] I. Skarmoutsos, D. Dellis, J. Samios, The effect of intermolecular interactions on local density inhomogeneities and related dynamics in pure supercritical fluids. A comparative molecular dynamics simulation study, J. Phys. Chem. B 113 (2009) 2783–2793.
[16] S.C. Tucker, Solvent density inhomogeneities in supercritical fluids, Chem. Rev. 99 (1999) 391–418.

[17] X. Nie, Z. Du, L. Zhao, S. Deng, Y. Zhang, Molecular dynamics study on transport properties of supercritical working fluids: literature review and case study, Appl. Energ. 250 (2019) 63–80.

[18] J.V Sengers, J.G. Shanks, Experimental critical-exponent values for fluids, J. Stat. Phys. 137 (2009) 857–877.

[19] J.M. Stubbs, Molecular simulations of supercritical fluid systems, J. Supercrit. Fluid. 108 (2016) 104–122.

[20] A.G. Kalinichev, Molecular dynamics and self-diffusion in supercritical water, Berichte Der Bunsengesellschaft Für Physikalische Chemie 97 (1993) 872–876.

[21] J. Nichele, A.B. de Oliveira, L.S. de B. Alves, I. Borges Jr, Accurate calculation of near-critical heat capacities CP and CV of argon using molecular dynamics, J. Mol. Liq. 237 (2017) 65–70.

[22] J. Nichele, I. Borges Jr, A.B. Oliveira, L.S. Alves, Molecular dynamics simulations of momentum and thermal diffusion properties of near-critical argon along isobars, J. Supercrit. Fluid. 114 (2016) 46–54.

[23] I. Shvab, R.J. Sadus, Thermophysical properties of supercritical water and bond flexibility, Phys. Rev. E 92 (2015), 12124.

[24] S. Marinakis, J. Samios, The temperature and density dependence of fluid xenon self-diffusion coefficients: a comparison between experimental, theoretical and molecular dynamics results, J. Supercrit. Fluid. 34 (2005) 81–89.

[25] P.W.E. Peereboom, H. Luijges, K.O. Prins, An NMR spin-echo study of self-diffusion in xenon, Phys. A 156 (1989) 260–276.

[26] P Atkins, J. Paula, Physical Chemistry Thermodynamics, Structure, and Change, WH Freeman and Company, New York, 2014.

[27] H.J.C. Berendsen, J.P.M. van Postma, W.F. van Gunsteren, A. DiNola, J.R. Haak, Molecular dynamics with coupling to an external bath, J. Chem. Phys. 81 (1984) 3684–3690.

[28] J.E. Jones, On the determination of molecular fields.—I. From the variation of the viscosity of a gas with temperature, Proceed. Royal Soc. London. Series A, Containing Papers of a Math. Phys. Character 106 (1924) 441–462.

[29] J.E. Lennard-Jones, Cohesion, proceedings of the physical society (1926-1948), 43 (1931) 461.

[30] W.W. Wood, F.R. Parker, Monte Carlo equation of state of molecules interacting with the lennard-jones potential. I. A supercritical isotherm at about twice the critical temperature, J. Chem. Phys. 27 (1957) 720–733.

[31] A. Rahman, Correlations in the motion of atoms in liquid argon, Phys. Rev. 136 (1964), A405.

[32] M.A. van der Hoef, P.A. Madden, Three-body dispersion contributions to the thermodynamic properties and effective pair interactions in liquid argon, J. Chem. Phys. 111 (1999) 1520–1526.

[33] H. Heinz, R.A. Vaia, B.L. Farmer, R.R. Naik, Accurate simulation of surfaces and interfaces of face-centered cubic metals using 12−6 and 9−6 Lennard-Jones potentials, J. Phys. Chem. C 112 (2008) 17281–17290.

[34] I.L. Geada, H. Ramezani-Dakhel, T. Jamil, M. Sulpizi, H. Heinz, Insight into induced charges at metal surfaces and biointerfaces using a polarizable Lennard–Jones potential, Nat. Commun 9 (2018) 1–14.

[35] X. Wang, S. Ramírez-Hinestrosa, J. Dobnikar, D. frenkel, The Lennard-Jones potential: when (not) to use it, Phys. Chem. Chem. Phys. 22 (2020) 10624–10633.

[36] P. Carlès, A brief review of the thermophysical properties of supercritical fluids, J. Supercrit. Fluid. 53 (2010) 2–11.

[37] M.W. Maddox, G. Goodyear, S.C. Tucker, Effect of critical slowing down on local-density dynamics, J. Phys. Chem. B 104 (2000) 6266–6270.

[38] H.L. Martinez, R. Ravi, S.C. Tucker, Characterization of solvent clusters in a supercritical Lennard-Jones fluid, J. Chem. Phys. 104 (1996) 1067–1080.

[39] N. Yoshii, S. Okazaki, Molecular dynamics study of structure of clusters in supercritical Lennard–Jones fluid, Fluid Phase Equilibr 144 (1998) 225–232.

[40] A. Idrissi, I. Vyalov, N. Georgi, M. Kiselev, On the characterization of inhomogeneity of the density distribution in supercritical fluids via molecular dynamics simulation and data mining analysis, J. Phys. Chem. B 117 (2013) 12184–12188.

[41] N. Metatla, F. Lafond, J.-P. Jay-Gerin, A. Soldera, Heterogeneous character of supercritical water at 400°C and different densities unveiled by simulation, RSC Adv. 6 (2016) 30484–30487.

[42] I. Skarmoutsos, E. Guardia, J. Samios, Local structural fluctuations, hydrogen bonding and tructural transitions in supercritical water, J. Supercrit. Fluid. 130 (2017) 156–164.

[43] Supercritical fluids: fundamentals and applications, Chem. Bus. 28 (2014) 45–48.

[44] P.E. Savage, Organic chemical reactions in supercritical water, Chem. Rev. 99 (1999) 603–621.

[45] C. Tegeler, R. Span, W. Wagner, A new equation of state for argon covering the fluid region for temperatures from the melting line to 700 K at pressures up to 1000 MPa, J. Phys. Chem. Ref. Data 28 (1999) 779–850.

[46] A. Michels, Wijker H, H.K. Wijker, Isotherms of argon between 0°C and 150°C and pressures up to 2900 atmospheres, Physica 15 (1949) 627–633.

[47] P.T. Cummings, Molecular Simulation of Near-Critical and Supercritical Fluids. Supercritical Fluids: Fundamentals for Applications, Kluwer Academic Publishers Dordrecht, 1994.

[48] S. Plimpton, Fast parallel algorithms for short-range molecular dynamics, J. Comput. Phys. 117 (1995) 1–19.

[49] D. Frenkel, B. Smit, Understanding Molecular Simulation: From Algorithms To Applications, Elsevier, 2001.

[50] K. Ghosh, C.V Krishnamurthy, Structural behavior of supercritical fluids under confinement, Phys. Rev. E 97 (2018), 12131.

[51] M.P. Allen, D.J. Tildesley, Computer Simulation of Liquids, Oxford university press, 2017.

[52] I. Skarmoutsos, J. Samios, Local density inhomogeneities and dynamics in supercritical water: A molecular dynamics simulation approach, J. Phys. Chem. B 110 (2006) 21931–21937.

[53] S. Nosé, A unified formulation of the constant temperature molecular dynamics methods, J. Chem. Phys. 81 (1984) 511–519.

[54] W.G. Hoover, Canonical dynamics: Equilibrium phase-space distributions, Phys. Rev. A 31 (1985), 1695.

[55] D.C. Rapaport, D.C.R. Rapaport, The Art of Molecular Dynamics Simulation, Cambridge university press, 2004.

[56] L. Sijie, B. Bofeng, Multi-vapor embryos nucleation process and spinodal analyses of expandable superheated water system, Nanosc. Microsc. Therm. 14 (2010) 174–185.

[57] A. Yamane, F. Shimojo, K. Hoshino, Effects of long-range interactions on the structure of supercritical fluid mercury: Large-scale molecular-dynamics simulations, J. Phys. Soc. Jpn. 75 (2006), 124602-124602.

[58] A.S. Raman, H. Li, Y.C. Chiew, Widom line, dynamical crossover, and percolation transition of supercritical oxygen via molecular dynamics simulations, J. Chem. Phys. 148 (2018), 014502.

[59] M.W. Maddox, G. Goodyear, S.C. Tucker, Origins of atom-centered local density enhancements in compressible supercritical fluids, J. Phys. Chem. B 104 (2000) 6248–6257.

[60] D.T. Banuti, Crossing the Widom-line–supercritical pseudo-boiling, J. Supercrit. Fluid. 98 (2015) 12–16.

[61] J. Xu, Y. Wang, X. Ma, Phase distribution including a bubblelike region in supercritical fluid, Phys. Rev. E 104 (2021), 14142.

[62] B. Senger, P. Schaaf, D.S. Corti, R. Bowles, J-C. Voegel, H. Reiss, A molecular theory of the homogeneous nucleation rate. I. Formulation and fundamental issues, J. Chem. Phys. 110 (1999) 6421–6437.

[63] J. Wedekind, D. Reguera, What is the best definition of a liquid cluster at the molecular scale? J. Chem. Phys. 127 (2007) 154516.

[64] P.R. ten Wolde, M.J. Ruiz-Montero, D. Frenkel, Numerical calculation of the rate of homogeneous gas–liquid nucleation in a Lennard-Jones system, J. Chem. Phys. 110 (1999) 1591–1599.

[65] J. Losey, R.J. Sadus, Structural behavior of fluids from the vapor and liquid region to the supercritical phase, Phys. Rev. E 100 (2019), 052132.

[66] P.R. ten Wolde, D. Frenkel, Computer simulation study of gas–liquid nucleation in a Lennard-Jones system, J. Chem. Phys. 109 (1998) 9901–9918.

[67] L.F. Vega, Perspectives on molecular modeling of supercritical fluids: From equations of state to molecular simulations. Recent advances, remaining challenges and opportunities, J. Supercrit. Fluid. 134 (2018) 41–50.

[68] H.E. Stanley, Introduction to Phase Transitions and Critical Phenomena, Oxford Univ. Press, 1971.

[69] J. Nichele, L.S.B. Alves, I. Borges Jr, Equation of state for near critical argon obtained via molecular dynamics, High Temp-High Press 43 (2014) 385–400.

[70] K. Saitow, K. Otake, H. Nakayama, K. Ishii, K. Nishikawa, Local density enhancement in neat supercritical fluid due to attractive intermolecular interactions, Chem. Phys. Lett. 368 (2003) 209–214.

[71] H.G. Schuster, W. Just, Deterministic Chaos: An Introduction, John Wiley & Sons, 2006.

[72] J. Qu, H. Wu, P. Cheng, X. Wang, Non-linear analyses of temperature oscillations in a closed-loop pulsating heat pipe, Int. J. Heat Mass Tran. 52 (2009) 3481–3489.
[73] S.M. Pincus, Approximate entropy as a measure of system complexity, P. Natl. Acad. Sci USA 88 (1991) 2297–2301.
[74] J.S. Richman, D.E. Lake, J.R. Moorman, Sample entropy, methods in enzymology, Academic Press 384 (2004) 172–184.
[75] S. Zurek, P. Guzik, S. Pawlak, M. Kosmider, J. Piskorski, On the relation between correlation dimension, approximate entropy and sample entropy parameters, and a fast algorithm for their calculation, Physica A 391 (2012) 6601–6610.
[76] T.D. Pham, H. Yan, Spatial-dependence recurrence sample entropy, Physica A 494 (2018) 581–590.